



A luminescent view of the clickable assembly of LnF_3 nanoclusters

Jie Zhou^{1,3}, Yang Wei^{1,3}, Yue Pan^{1,2}, Yue Wang¹, Ze Yuan¹, Fan Zhang¹, Hao Song¹, Jingyi Yue¹, Haiquan Su², Xiaoji Xie¹  [✉] & Ling Huang¹  [✉]

Nanoclusters (NCs) bridge the gap between atoms and nanomaterials in not only dimension but also physicochemical properties. Precise chemical and structural control, as well as clear understanding of formation mechanisms, have been important to fabricate NCs with high performance in optoelectronics, catalysis, nanoalloys, and energy conversion and harvesting. Herein, taking advantage of the close chemical properties of Ln^{3+} ($\text{Ln} = \text{Eu}, \text{Nd}, \text{Sm}, \text{Gd}, \text{etc.}$) and Gd^{3+} - Eu^{3+} energy transfer ion-pair, we report a clickable LnF_3 nanoparticle assembly strategy allowing reliable fabrication of diversely structured NCs, including single-component, dimeric, core-shelled/core-shell-shelled, and reversely core-shelled/core-shell-shelled, particularly with synergized optical functionalities. Moreover, the purposely-embedded dual luminescent probes offer great superiority for in situ and precise tracking of tiny structural variations and energy transfer pathways within complex nanoarchitectures.

¹Institute of Advanced Materials (IAM), Nanjing Tech University, 30 South Puzhu Road, Nanjing, China. ²School of Chemistry and Chemical Engineering, Inner Mongolia University, 235 West Daxue Road, Hohhot, China. ³These authors contributed equally: Jie Zhou, Yang Wei. ✉email: iamxjie@njtech.edu.cn; iamlhuang@njtech.edu.cn

Organic ligands have played an irreplaceable role in myriads of nanomaterials synthesis towards control of size^{1,2}, morphology^{3,4}, crystal structure⁵, and functionality^{6,7}. Meanwhile, rational selection of the chemical groups on ligand molecules is also critical for post-modulations such as assembly, hybridization, and fabrication of micro or macroscaled architectures from individual nanoparticles (NPs) aiming at unprecedented chemical and physical properties^{8,9}, particularly when other technologies such as Langmuir–Blodgett^{10,11}, layer-by-layer¹², and optical or electron-beam lithography are combined^{13,14}.

Moreover, development of a library of ligand exchange methods through nanoscale chemical reactions has facilitated easy conversion of nanomaterials from hydrophobic to hydrophilic or vice versa^{15–17}, which generates additional functionalities to realize various purposes such as QLED display¹⁸, trace analysis¹⁹, disease diagnosis²⁰, bioimaging²¹, as well as photodynamic therapy²², and so on. As a typical example, replacement of citrate ligand on gold NPs with thiol-ended single chain DNA has enabled successful assembly of gold NPs possessing complementary DNA sequences, which leads to precise fabrication of supercrystals with varied lattice structures²³ and remarkable features that neither individual component possesses^{24,25}.

However, ligand molecules may also affect or even prevent functionality expression. For example, insulating molecules are unwanted for semiconducting quantum dots when used for nanodevice fabrication²⁶, chemical molecules surrounding perovskite nanocrystals usually exacerbate the optoelectronic performance in therein fabricated solar cells²⁷, and catalytic noble metal NPs get poisoned by organic molecules used as protecting ligands and so do for the photo- and/or electrochemical catalysis²⁸. On the other side, aggregation of nanomaterials occurs once ligands are removed, accompanied with irreversible functionality loss. Thus, it remains an urgent challenge to find an optimal balance between this dilemma, that is, how to fully exploit the functionalities of nanomaterials that are prone to aggregation once without ligand and meanwhile avoid the influence of ligand molecules, particularly for tiny NPs (<5 nm) that are very active due to the high surface energy²⁹.

Herein, we have developed a clickable assembly strategy that facilitates reliable fabrication of variously structured lanthanide nanoclusters (NCs) with synergized multi-functionalities. The formation of LnF₃ NCs starts with conversion of LnOF NPs to LnF₃ NPs after organic ligand removal, followed by the assembly process. This HCl-triggered click-reaction allows arbitrary fabrication of the compositions and structures of target NCs such as single-component, dimeric, core-shelled/core-shell-shelled, and reversely core-shelled/core-shell-shelled. The embedded dual luminescent probes via either dynamic energy transfer (Gd³⁺–Eu³⁺) or direct excitation (of Eu³⁺) enables sensitive track of tiny variations in structure and energy transfer pathways.

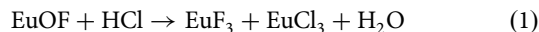
Results

Assembly of EuOF NPs into EuF₃ NCs. Specifically, addition of certain amount of diluted HCl into the stock solution of EuOF NPs (Fig. 1a and Supplementary Fig. 1) strips off majority of the oleic acid anion (OA[−]) ligands and almost simultaneously triggers the conversion to small EuF₃ NPs (Fig. 1b). The coordination between surface Eu³⁺ on EuF₃ NPs and solvent molecules (H₂O or C₂H₅OH)³⁰ improves the solubility. Although these consequent nanoscaled-rare earth chemical reactions complete within 5 mins, they describe exactly why the solution changes from opaque to transparent after HCl addition (Supplementary Fig. 2a, b). However, EuF₃ NPs are metastable due to high surface energy and finally assemble into stable NCs through a random attachment mechanism (Fig. 1c, d, Supplementary Fig. 3 and

Supplementary Fig. 4). The reason we speculate that the final solution turned back from transparent to opaque (Supplementary Fig. 2c) is that, the trace amount of OA[−] left on each EuF₃ NP gradually accumulated on NCs surface when assembly progresses, which leads to increased hydrophobicity and thus decreased solubility in ethanol (Fig. 1c).

Based on systematic analysis of TEM (Fig. 2a–h) and FT-IR (Fig. 2i) results of the samples collected at different assembly times, the growth process of EuF₃ NCs can be divided into the following three stages:

Stage 1: Conversion of EuOF NPs to EuF₃ NPs. This is the most critical step, which forms the foundation for subsequent assembly and growth of EuF₃ NCs. TEM images (Fig. 2a–c and Supplementary Fig. 5) suggest that EuOF NPs at diameter of 3.2 nm turned into semi-dissociated morphologies after 1 min of H⁺ addition, which is caused by the ligands (OA[−]) removal induced by the post-added H⁺^{30,31}. Then, chemical conversion of EuOF NPs to EuF₃ NPs occurred, which can be explained by the theory of hard and soft acids and bases (HSAB)³². The so called “hard” acids and “hard” bases prefer to bond with each other, and so do the “soft” acids and “soft” bases. In our reaction system, F[−] ion as a base is harder than O^{2−} and similarly H⁺ as an acid is harder than Eu³⁺. Therefore, the Eu–O bond was broken under the attack of H⁺, which results in the semi-dissociation of EuOF NPs and release of non-bonded Eu³⁺ and F[−] ions. Then Eu³⁺ preferentially bonds with F[−] rather than O^{2−} by forming tiny EuF₃ NPs³³. The chemical equation can be expressed as:



Moreover, disappearance of FT-IR peaks at ~2923, 2852, 1560 and 1466 cm^{−1} clearly indicates debond of OA[−] ligands from surface Eu³⁺. The conversion of EuOF NPs to EuF₃ NPs completes at reaction time of 5 min (Supplementary Fig. 5). This is also consistent with the change of solution from opaque to transparent at 5 min (Supplementary Fig. 2), which is due to the improved solubility of EuF₃ NPs through solvent molecule (H₂O or C₂H₅OH) coordination, as proved by the broad hydroxyl peak at ~3400 cm^{−1} (ref. ³⁴) (Fig. 2i).

Stage 2: Initiation of the assembly. Presence of OA[−] improves solubility and mitigates collision probability of NPs in solution, which allows long-term storage of LnOF NPs precursors without worrying about aggregation (Supplementary Fig. 1). However, surface ions become exposed once OA[−] is removed, causing sharply risen surface energy of EuF₃ NPs²⁹ and initiates the assembly (Fig. 2c).

Stage 3: Growth of EuF₃ NCs. The size of EuF₃ NCs grew from 3.1 to 21.8, 29.2, 35.7, 38.4, and 40.1 nm at the assembly time of 15, 30, 60, 120, 240, and 360 min, respectively (Fig. 2c–h, j and Supplementary Fig. 6). Parallely, the FT-IR peaks at 2852 and 2923 cm^{−1} corresponding to –CH₃ stretching vibration intensified from almost nil at 5 min to that of 30 min and further at 360 min (Fig. 2i). This is reasonable because trace amount of OA[−] on the surface of individual EuF₃ NP can't produce sufficient FT-IR signal at stages 1 and 2. More and more ligands are accumulated (Fig. 1c, d) when NCs grow larger as assembly progresses, resulting in stronger signals. This also well agrees with the solubility change in ethanol solution from transparent to opaque (Supplementary Fig. 2b, c). Thus, the intensity variation of FT-IR peaks at 2852 and 2923 cm^{−1} (Fig. 2i) could qualitatively unveil the structural details of NCs formed at different assembly stages.

Driving force for EuF₃ NCs assembly. As previously reported³⁵, multiple interactions usually work together to make for the final structure of assemblies. In our case, removal of surface ligands from NPs not only exposes a large number of uncoordinated Eu³⁺, but

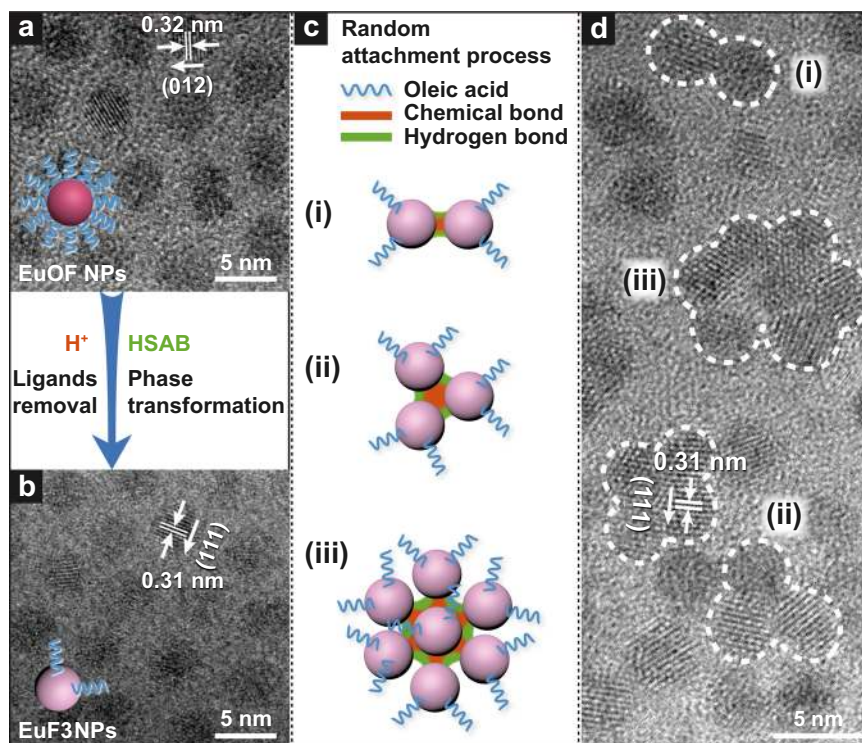


Fig. 1 Self-assembly mechanism of NCs. High-resolution transmission electron microscope (HRTEM) images of **a** EuOF NPs and **b** EuF₃ NPs. **c** Schematic diagram illustrating the structural details, random attachment process, and interaction forces responsible for NCs formation. **d** HRTEM image taken at assembly time of 15 min. The insets in **a** and **b** enlighten the difference of the number of ligand molecules after H⁺ introduction. TEM structures of (i), (ii), and (iii) in **d** correspond exactly to those in **c**.

also leads to increased surface energy. In this situation, unstable EuF₃ NPs tend to contact and attach with each other to decrease the total energy through interparticle interactions, and eventually assemble into NCs. The FT-IR peak at 3400 cm⁻¹ implies the existence of hydrogen bond among solvent molecules, while the partially fused crystal lattices (Fig. 1d) suggest the formation of Eu-F chemical bond among EuF₃ NPs, both of which are the main interactions responsible for the assembly of EuF₃ NCs through a random attachment process (Fig. 1c, d). Moreover, as widely reported^{36,37}, dipole-induced interaction is a strong force at the nanoscale to drive self-assembly, which usually occurs in NPs with asymmetric crystal lattice. Considering the trigonal crystal structure of EuF₃ NPs with relatively low symmetry among the seven crystal systems and the big difference in electronegativity between F⁻ and Eu³⁺, there might exist electric dipole moment originated from the polarity of crystal lattice of EuF₃ NPs, which may generate dipole-dipole interactions between EuF₃ NPs and act as a driving force for the self-assembly process.

More intriguingly, although the as-assembled EuF₃ NCs are polycrystalline, they are readily to be converted into single crystals when annealed at temperatures as low as 50 °C (Supplementary Fig. 7). This principle might be instructive to the synthesis of nanocrystals or nanoalloys that are not possible at nearly room temperature. Moreover, NCs of NdF₃, SmF₃, and GdF₃ were also successfully constructed by following the same strategy (Supplementary Figs. 8 and 9).

Working principle of Eu³⁺ as luminescent probe. As two major photoluminescence (PL) emissions in Eu³⁺, the intensity at 612 nm corresponding to the ⁵D₀→⁷F₂ electric dipole transition (I_E) is highly sensitive to the local site symmetry while that of the ⁵D₀→⁷F₁ magnetic dipole transition (I_M) at 591 nm is not³⁸ (Fig. 3a). Considering that local site symmetry of luminescent

ions, here means Eu³⁺, usually links with surface coordination environment, evolution of the value of I_E/I_M may be used as a luminescent probe to track the changes of the proportion of surface Eu³⁺ in different assemblies (Fig. 3a, b and Supplementary Table 1). Indeed, when excited at the characteristic working wavelength of Eu³⁺ (395 nm), the calculated I_E/I_M decreases gradually from 3.80 in EuF₃ NPs to 1.14 in EuF₃ NCs, indicating that the amount of surface Eu³⁺ keeps reducing with the size increase of NCs (Fig. 3b, c)³⁹. This well-agrees with the mergence of NPs when forming NCs, which causes reduced surface area (Figs. 1d and 3a).

It is worth pointing out that the gradually decrescent full-width at half maximum (FWHM) at 591 nm is due to the increased site symmetry of Eu³⁺ during NCs growth³⁸. Generally, the crystallographic site symmetry significantly affects the spectral line-width of Eu³⁺, and a minor structural distortion may alter the crystal field symmetry of Eu³⁺, which will be reflected by the gradual change of FWHM from 12.1 to 7.2 nm as the NCs grow from 3.1 to 40.1 nm^{40,41}.

Construction of arbitrarily designed NCs. Clear understanding of the NC formation mechanisms, particularly the information extracted from luminescent probe has inspired us to further fabricate more complicated NCs and explore their structural relationships with the evolution of I_E/I_M. Instead of the above uninterrupted NC assembly (Fig. 2), the conversion of LnOF NPs to and the following assembly of LnF₃ NPs were purposely separated, which offers more freedom to grow NCs with widely varied structures and pre-designed chemical compositions. For example, dimeric NCs of EuF₃&GdF₃ and EuF₃&2GdF₃ could be reliably constructed by simply mixing NPs of EuF₃ and GdF₃ that were pre-converted from EuOF and GdOF NPs via a H⁺-induced clickable reaction, at molar ratios of 1:1 and 1:2, respectively

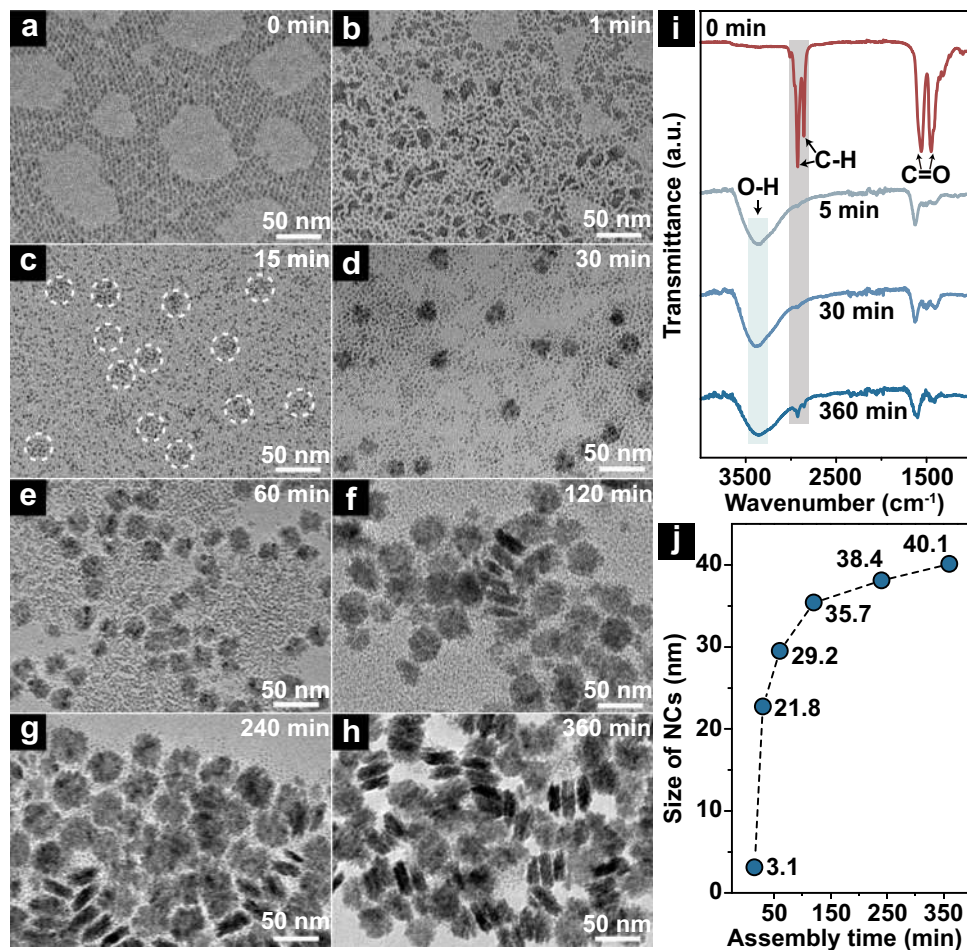


Fig. 2 Different assembly stages of NCs. TEM images of the products obtained at assembly time of **a** 0, **b** 1, **c** 15, **d** 30, **e** 60, **f** 120, **g** 240, and **h** 360 min, respectively. **i** FT-IR spectra of the products obtained at the assembly time of 0, 5, 30, and 360 min, respectively. **j** Time-dependent size evolution of NCs. White dotted-circles in **c** show the NCs formed at very early stage.

(Fig. 4a–c). Similarly, core-shelled NCs of $\text{EuF}_3@GdF_3$ and $\text{EuF}_3@GdF_3@GdF_3$ could also be fabricated by controlling the number of GdF_3 shells grown on pre-formed core of EuF_3 NCs (Fig. 4d–f) and alternatively, the reversely core-shelled NCs of $GdF_3@EuF_3$ and $GdF_3@EuF_3@EuF_3$ were further grown by reversing the assembly sequence of respective components (Fig. 4g–i).

Luminescent probes for tracking of structural variations and energy transfer pathways. Compared with previous assembly mechanism studies where HRTEM, XRD, and synchrotron characterizations were heavily relied^{42,43}, information provided by luminescent probes can be in situ, dynamic, precise, and particularly sensitive to its surrounding environment. Indeed, as depicted in Fig. 4, different $Gd^{3+}-Eu^{3+}$ energy transfer modes were clearly distinguished in their respective PL spectral evolution, which could be utilized to track the distribution variation of surface Eu^{3+} on NCs with different structures.

For pure EuF_3 NCs, there is only very weak PL because Eu^{3+} has almost no absorption at 273 nm (Supplementary Fig. 10a, b). However, a 70-fold emission enhancement (Fig. 5a) was seen in $\text{EuF}_3@GdF_3$ NCs, which is rational because 273 nm is the characteristic working wavelength of Gd^{3+} and more energy is transferred to Eu^{3+} in the co-assembled NCs (Fig. 4b and Supplementary Fig. 11). Subsequently, a 103-fold PL enhancement was obtained in $\text{EuF}_3@2GdF_3$ NCs due to further increased energy transfer from Gd^{3+} to Eu^{3+} (Fig. 4c). Consistently, the characteristic

absorption peak of Gd^{3+} at 273 nm appeared in $\text{EuF}_3@GdF_3$ and became stronger in $\text{EuF}_3@2GdF_3$, proving the successful assembly of GdF_3 NPs at increased amount (Supplementary Fig. 10a). More excitingly, such PL evolution also agrees with the gradually intensified optical images of respective samples (Supplementary Fig. 12a) under 273 nm light excitation where $\text{EuF}_3@2GdF_3$ is the brightest. Correspondingly, the lifetime of Eu^{3+} (Fig. 5a and Supplementary Fig. 13a) shows similar trend of increase from EuF_3 NPs (0.59 ms) to $\text{EuF}_3@GdF_3$ (1.46 ms) as that from $\text{EuF}_3@GdF_3$ (1.46 ms) to $\text{EuF}_3@2GdF_3$ (2.12 ms). As a stark contrast, neither emission intensity nor lifetime change was observed in Eu^{3+} under 273 nm light excitation (Supplementary Fig. 14) when solutions containing pre-formed NCs of GdF_3 and EuF_3 were physically mixed at the atomic ratios of 2:1, 1:1, and 0:1, respectively. This proves straightforwardly that $Gd^{3+}-Eu^{3+}$ energy transfer can hardly occur if without uniform co-assembly between EuF_3 and GdF_3 NPs (Fig. 4a–c).

Similarly, Gd^{3+} in GdF_3 shell keeps transferring energy to internal Eu^{3+} , resulting in enhanced PL in $\text{EuF}_3@GdF_3$ NCs (Fig. 5b and Supplementary Fig. 10c, d). However, it is reasonable to see only 2.5-fold enhancement because there exists partial energy loss from surface Gd^{3+} on GdF_3 shell (Fig. 4e). Indeed, an enhancement of 6.5 folds is seen in $\text{EuF}_3@GdF_3@GdF_3$ NCs, which is due to: 1) increased amount of Gd^{3+} that transfers more energy to Eu^{3+} and meanwhile, 2) decreased amount of Gd^{3+} energy loss due to the growth of the second GdF_3 shell (Fig. 4f). Accordingly, there is a larger Eu^{3+} lifetime increase (Fig. 5b and

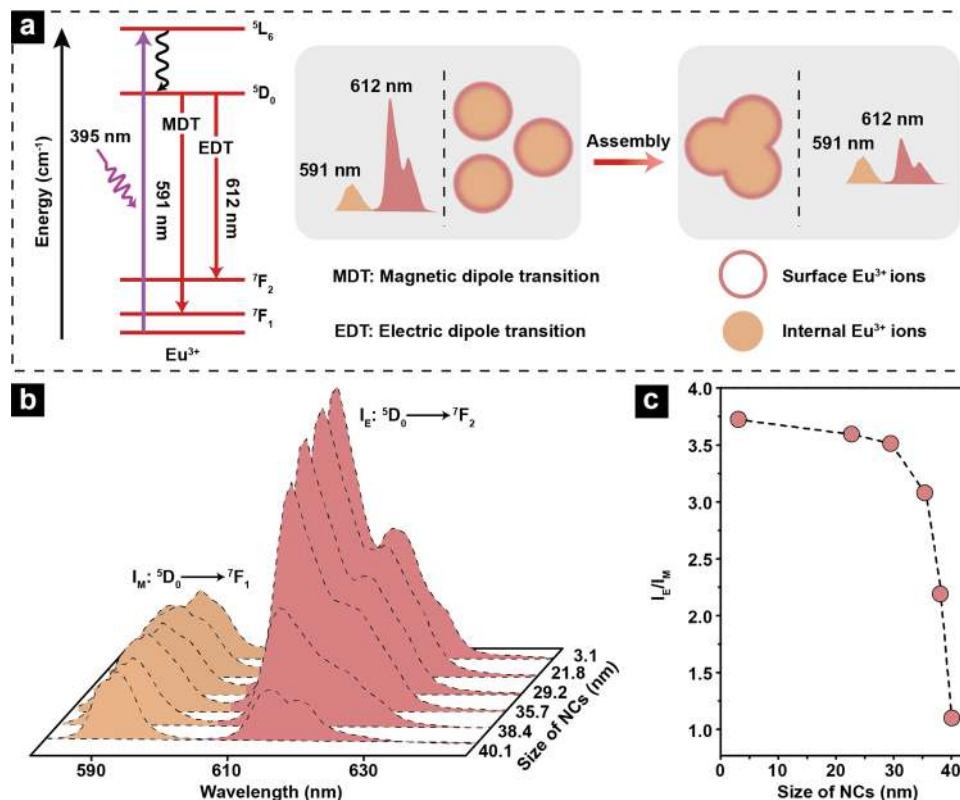


Fig. 3 Working principle of Eu^{3+} used as luminescent probe. **a** Illustration of different electron transition pathways in Eu^{3+} and intensity evolutions of electric-dipole (612 nm) and magnetic-dipole (591 nm) transitions during NCs growth. **b** Evolution of PL spectra and **c** I_E/I_M value of Eu^{3+} in NCs with different sizes. 395 nm light was used as excitation source.

Supplementary Fig. 13b) after growth of the second GdF_3 shell (from 1.07 to 2.43 ms) compared with that of the first GdF_3 shell (from 0.59 to 1.07 ms).

Interestingly, more enhanced (7.3-fold) PL is seen in $\text{GdF}_3@EuF_3$ NCs than that of 2.5-fold in $EuF_3@GdF_3$ NCs (Fig. 5b, c and Supplementary Fig. 10e, f). This is due to more efficient energy transfer from internal Gd^{3+} to exterior Eu^{3+} where energy loss in Fig. 4e was largely impressed in Fig. 4h. However, the reason that only 8.1-fold PL enhancement is gained after growth of a second EuF_3 shell is because the amount of energy transferred from Gd^{3+} is fixed so that the second layer of Eu^{3+} can only absorb the extra energy that passes through the first Eu^{3+} shell (Fig. 4i). Rationally, the lifetime increase of Eu^{3+} (Fig. 5c and Supplementary Fig. 13c) is not as much after growth of the second EuF_3 shell (from 1.33 to 1.61 ms) compared with that of the first (from 0.59 to 1.33 ms). It is worth emphasizing that the calculated quantum yields^{39,44} of EuF_3 (Supplementary Equation (1) and Supplementary Table 2) are consistent with above-discussed PL intensity evolution, and variation of the calculated GdF_3 - EuF_3 energy transfer rate^{45–48} in different NCs based on simplified models (Supplementary Fig. 15) provides further support to our schematic illustrations in Fig. 4.

To dig out more structural information from another point of view, the PL evolution in different NCs was investigated by directly exciting Eu^{3+} at 395 nm (Supplementary Fig. 16). For easy comparison, the PL intensity in pure EuF_3 NCs was set at 1.0 and the calculated enhancement factors in different NCs were shown in Fig. 5d–f. It is reasonable to see enhanced PL in $EuF_3@GdF_3$ and $EuF_3@2GdF_3$ because there exists a Eu^{3+} - Eu^{3+} energy migration loop (Supplementary Fig. 16a and Supplementary Fig. 17a–c) in pure EuF_3 NCs⁴⁹ that deteriorates the emission while insertion of co-assembled GdF_3 NPs breaks the loop and

leads to enhanced PL in $EuF_3@GdF_3$. It is also reasonable to see a 2.6- and 2.0-fold enhancement because the unit number of Eu^{3+} is diluted 2 and 3 times in $EuF_3@GdF_3$ and $EuF_3@2GdF_3$ (Fig. 5d), respectively. In another word, there shall be a 5.2- and 6-fold absolute PL enhancement in $EuF_3@GdF_3$ and $EuF_3@2GdF_3$, respectively. This phenomenon is quite instructive for materials design towards maximized PL intensity while minimizing the amount of activators used. Parallely, the lifetime of Eu^{3+} also increases from 0.62 to 1.49, and 2.08 ms (Supplementary Fig. 16b).

Growth of a GdF_3 shell suppresses the energy loss of surface Eu^{3+} similar to that of Gd^{3+} in Fig. 4e and results in 3.6-fold PL enhancement in $EuF_3@GdF_3$, while the 6.0-fold PL enhancement in $EuF_3@GdF_3@GdF_3$ suggests that the second shell has even better energy loss suppression (Supplementary Fig. 16c). This is also consistent with the lifetime increase of Eu^{3+} from 0.62 to 1.05, and 2.40 ms (Supplementary Fig. 16d). Alternatively, growth of a EuF_3 shell around pre-formed core of GdF_3 NCs results in larger inter-particle distance, which generates similar (3.8-fold) effect as that in $EuF_3@GdF_3$ (Supplementary Fig. 17a–c), that is, the broken energy migration loop and enhanced PL (Supplementary Fig. 17a, d and e). Growth of the second EuF_3 shell not only suppresses the energy loss of Eu^{3+} in the first EuF_3 shell, the increased amount of Eu^{3+} generates extra PL so that a total enhancement of 6.7-fold is obtained in $\text{GdF}_3@EuF_3@EuF_3$ NCs (Supplementary Fig. 16e). Accordingly, the lifetime of Eu^{3+} increases from 0.62 to 1.35 and 1.65 ms (Fig. 5f and Supplementary Fig. 16f).

Moreover, based on the principle discussed in Fig. 3a, evolution of I_E/I_M value directly links with the variation of surface Eu^{3+} proportion in different NCs where tiny structural difference may be precisely probed. Indeed, for $EuF_3@GdF_3$ NCs with different EuF_3/GdF_3 molar ratios, the I_E/I_M remains almost constant

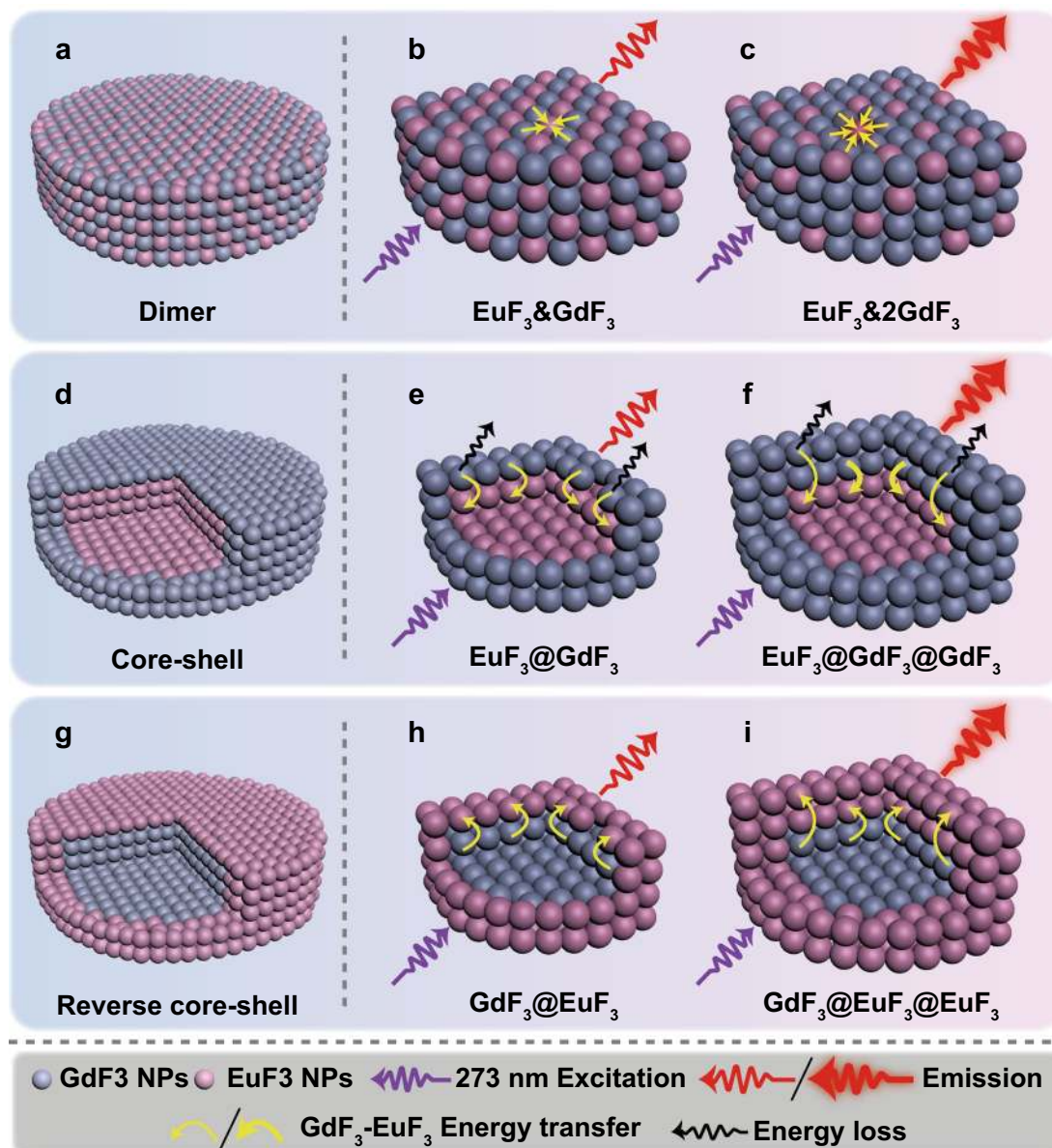


Fig. 4 Schematic illustration of the structures and energy transfer pathways of different NCs. The structures of **a** dimeric, **b** $\text{EuF}_3\&\text{GdF}_3$, and **c** $\text{EuF}_3\&2\text{GdF}_3$ NCs. **d** Core-shelled, **e** $\text{EuF}_3\text{@GdF}_3$, and **f** $\text{EuF}_3\text{@GdF}_3\text{@GdF}_3$ NCs. **g** Reversely core-shelled, **h** $\text{GdF}_3\text{@EuF}_3$, and **i** $\text{GdF}_3\text{@EuF}_3\text{@EuF}_3$ NCs, as well as their respective energy transfer pathways. **b**, **c**, **e**, **f** and **h**, **i** illustrate the energy transfer details in differently structured NCs using 273 nm light to excite Gd^{3+} , which transfers energy to Eu^{3+} (Supplementary Fig. 11). Note: for simplicity, energy migrations between $\text{Gd}^{3+}\text{-Gd}^{3+}$ and $\text{Eu}^{3+}\text{-Eu}^{3+}$ were not shown.

(Fig. 5g), which is reasonable because EuF_3 and GdF_3 NPs are mixed uniformly during co-assembly process. So, no matter what the $\text{EuF}_3/\text{GdF}_3$ molar ratio is, the proportion of surface Eu^{3+} compared to internal Eu^{3+} remains unchanged, which agrees exactly with the proposed structure in Fig. 4a.

Similarly, compared with pure EuF_3 NCs, growth of external GdF_3 shell sharply reduces the proportion of surface Eu^{3+} , so I_E/I_M value declined rapidly from 1.10 in EuF_3 NCs to 0.87 in $\text{EuF}_3\text{@GdF}_3$ and further to 0.78 in $\text{EuF}_3\text{@GdF}_3\text{@GdF}_3$ (Fig. 5h). The I_E/I_M value of Eu^{3+} also declined (Fig. 5i) from 1.10 in EuF_3 NCs to 1.00 in $\text{GdF}_3\text{@EuF}_3$ NCs and 0.92 in $\text{GdF}_3\text{@EuF}_3\text{@EuF}_3$ NCs because enlarged NCs shows lower proportion of surface Eu^{3+} .

Although TEM images only show morphological and dimensional differences of the above NCs (Supplementary Figs. 18, 19 and 20), the elemental mapping results provide unambiguous

evidence for the structural differences of the purposely fabricated NCs illustrated in Fig. 4. For example, uniform distribution of Eu and Gd signals in the structure of $\text{EuF}_3\&2\text{GdF}_3$ (Fig. 6a) suggests the complete co-assembly of EuF_3 and GdF_3 NPs, as depicted in Fig. 4c. Similarly, the opposite Eu and Gd signal distribution in Fig. 6b and c perfectly matches the core-shelled structure of $\text{EuF}_3\text{@GdF}_3\text{@GdF}_3$ (Fig. 4d) and reversely core-shelled structure of $\text{GdF}_3\text{@EuF}_3\text{@EuF}_3$ (Fig. 4g), respectively. These results are also highly consistent with both our principle designs and the structural details extracted from PL signals generated by the embedded dual luminescent probes of Gd^{3+} and Eu^{3+} .

Discussion

We have developed a clickable assembly strategy that allows facile construction of arbitrary NCs from individual LnF_3 NPs. As a

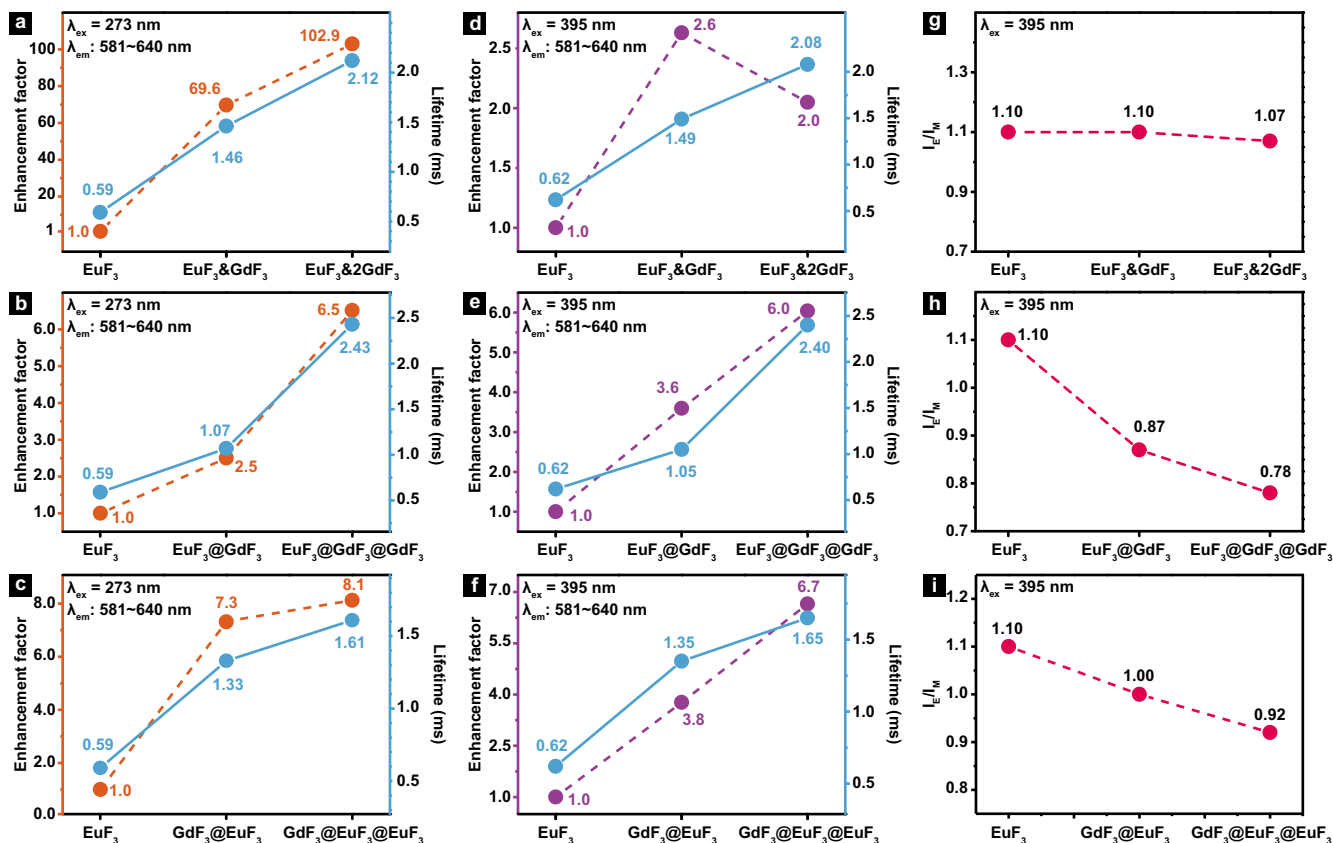


Fig. 5 The PL evolution in different-structured NCs. **a-c** Variation of luminescence enhancement factor (orange lines) and lifetime (baby blue lines) of Eu³⁺ in different NCs under 273 nm light excitation, through Gd³⁺-Eu³⁺ energy transfer. **d-f** Luminescence enhancement factor (purple lines) and lifetime (baby blue lines) of Eu³⁺ in different NCs under 395 nm light excitation. **g-i** Normalized I_E/I_M value of Eu³⁺ in different NCs.

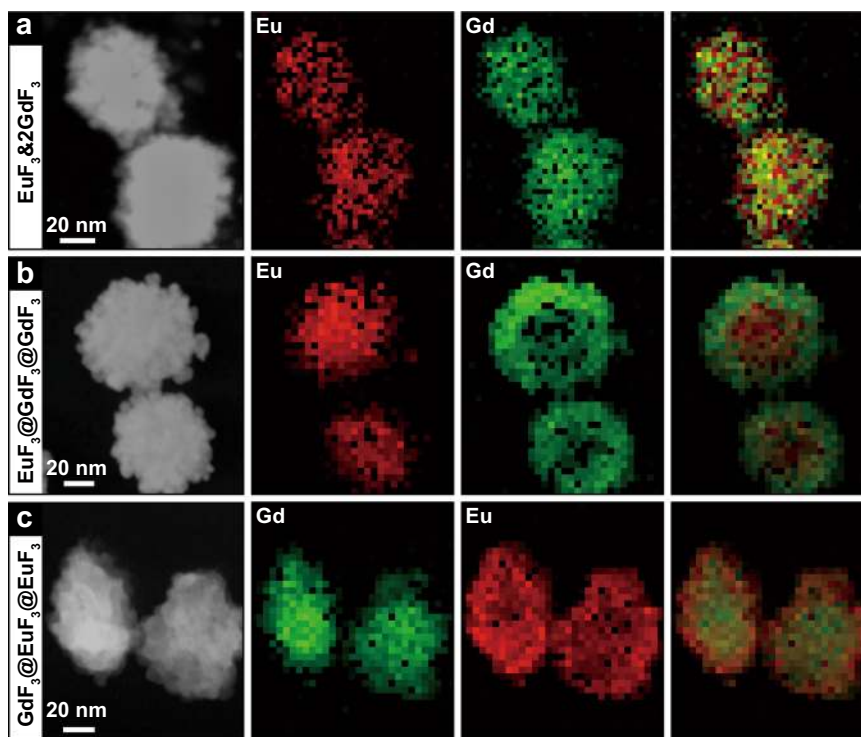


Fig. 6 Structural details of different NCs. High-angle annular dark-field scanning TEM images and corresponding energy-dispersive X-ray elemental mapping results of **a** EuF₃&2GdF₃ dimeric, **b** EuF₃@GdF₃@GdF₃ core-shelled, and **c** GdF₃@EuF₃@EuF₃ reversely core-shelled NCs.

complement to widely used one-step assembly, this two-step method enables fabrication of more versatile nanoarchitectures such as clusters, dimers, core-shells, and more importantly with multiple components and tunable functionalities without worrying about aggregation of precursors. It is worth emphasizing that the in-situ, sensitive, and dynamic PL signal generated by the embedded luminescent probes offers unparalleled superiority in precisely tracking not only tiny structural variations of but also energy transfer pathways in complex nanoarchitectures. Considering the large family of OA-stabilized NPs and principally other systems, this work has paved a potential avenue to the fabrication of widely diversified NCs with promising functionalities in the areas of catalysis, optoelectronics, energy conversion/harvesting, nanoalloys, bioimaging, as well as theranostics.

Methods

Materials. Oxides of Ln_2O_3 (99.99%, Ln = Eu, Gd, Sm, and Nd) were purchased from Beijing HWRK Chem. Co. LTD. Oleic acid (OA, 90%) and oleylamine (OM, 70%) were purchased from Sigma-Aldrich. Trifluoroacetic acid (TFA) and hydrochloric acid (HCl) was purchased from Shanghai Lingfeng Chemical Company, China. All the chemicals were used as received without further purification.

Preparation of $\text{Ln}(\text{CF}_3\text{COO})_3$. In a typical synthesis, lanthanide oxide was added into the aqueous solution containing slightly excessive trichloroacetic acid with continuous stirring, which was then kept refluxing so as to form an optically transparent solution. The resulting solution was filtered to remove the insoluble materials (if any), and the following solution was dried in an oven at 85 °C for 24 h to obtain $\text{Ln}(\text{CF}_3\text{COO})_3$.

Synthesis of LnOF NPs. Typical procedure: a given amount of $\text{Ln}(\text{CF}_3\text{COO})_3$ (2 mmol) was added into the mixture of OA (20 mmol) and OM (20 mmol) in a three-necked flask (100 mL) at room temperature. The slurry was heated to 100 °C with vigorous magnetic stirring under vacuum for 10 min in a temperature-controlled electromantle to remove water and oxygen, thereby forming an optically transparent solution, which was then ramped to 310 °C at a heating rate of 10 °C/min and maintained for 2 h under N_2 atmosphere. When cooling down to room temperature, the NPs were precipitated by adding excessive absolute ethanol into the reaction solution, followed by washing with ethanol for three times. Then the as-prepared NPs were dispersed into cyclohexane for further use.

Self-assembly of LnOF NPs into LnF_3 NCs. The NCs assembled from LnOF NPs were obtained through an acid treatment process. Typically, a certain amount of LnOF NPs and GdOF NPs were transferred into 4 mL ethanol solution, which was then poured into a 20 mL beaker and stirred for 5 min. 200 μL diluted hydrochloric acid solution (1 M) was added into the above solution and stirred at around 1000 r/min. After 6 h, the assembled NCs were generated in the solution, which was centrifuged at a speed of 8000 r/min for 4 min to obtain the NC samples, and then washed twice with ethanol under this condition to obtain the final NC samples.

Self-assembly of EuF_3 & GdF_3 dimeric NC. Take the EuF_3 & GdF_3 dimeric NC (molar ratio of EuF_3 : GdF_3 = 1:1) as an example: typically, a certain amount of EuOF NPs and GdOF NPs were transferred into 4 mL ethanol solution, respectively, which was poured into 20 mL beaker, and stirred for 5 min for complete dispersion. Then, 200 μL diluted hydrochloric acid solution (1 M) was added respectively into the above EuOF and GdOF solutions and kept stirring at around 500 r/min. After 10 min, the EuOF NPs and GdOF NPs totally converted into EuF_3 NPs and GdF_3 NPs, respectively. Then, solutions of EuF_3 NPs and GdF_3 NPs were mixed together into 20 mL beaker, and stirred at 1000 r/min. After 6 h, the above solution was centrifuged at a speed of 8000 r/min for 4 min to obtain the EuF_3 & GdF_3 dimeric NCs, which were then washed with ethanol twice under this condition to obtain the final products.

Self-assembly of core-shelled NCs. Take the EuF_3 @ GdF_3 core-shelled NCs (molar ratio of EuF_3 : GdF_3 = 1:1) as an example: typically, a certain amount of EuOF NPs was transferred into 4 mL ethanol solution, poured into 20 mL beaker, and stirred for 5 min. 200 μL diluted hydrochloric acid solution (1 M) was then added into the above solution and kept stirring for 6 h, until the assembled EuF_3 NCs were formed. The such-obtained EuF_3 NCs were further used as core for EuF_3 @ GdF_3 core-shell structured NCs growth. Meanwhile, a certain amount of GdOF NPs was transferred into 4 mL ethanol solution, poured into 20 mL beaker, and stirred for 5 min. Subsequently, 200 μL diluted hydrochloric acid solution (1 M) was added into the above GdOF solution and kept stirring for 10 min, until GdOF NPs totally converted into GdF_3 NPs. Then, solutions containing GdF_3 NPs and EuF_3 NCs were mixed together at certain ratio, and stirred for 6 h. The

solution was centrifuged at 8000 r/min for 4 min to obtain the EuF_3 @ GdF_3 core-shelled NCs, which were then washed twice with ethanol for future analysis.

Characterization. Powder X-ray diffraction (XRD) analysis was carried out on a Rigaku Smartlab (3 kW) X-ray diffractometer (Rigaku Corporation, Japan) using Cu K α radiation (λ = 1.5406 Å) and the measurement was performed at ambient temperature in the range of 2θ = 10–60 degree with 0.02 degree/step. Transmission electron microscope (TEM) images were recorded on a JEOL-1400 Plus (JEOL Ltd, Japan) at an acceleration voltage of 120 kV. High-resolution TEM (HRTEM) images and Energy-dispersive X-ray (EDX) spectra were obtained on a Tecnai G2 F20 TEM (FEI, America) at an acceleration voltage of 200 kV.

Fourier transform infrared (FT-IR) spectra were collected on a Nicolet 380 FT-IR spectrometer (Nicolet, America). Photoluminescence (PL) emission spectra were recorded on an Edinburgh FLS1000 Photoemission Spectrometer (Edinburgh Instruments, UK). All luminescent characterizations including PL emission spectra, excitation spectra, and luminescence decay curves were collected at 25 °C. Excitation and emission spectra were measured by using a 450 W continuous xenon arc lamp for sample excitation, and detailed parameters are shown in Supplementary Table 1. Luminescence decay curves were measured by using a compact 60 W xenon flash lamp ($\mu\text{F}2$) as excitation source with the frequency of 40 Hz.

Data availability

All data supporting the findings of this study are available within the paper and its supplementary information files.

Received: 24 June 2020; Accepted: 7 April 2021;

Published online: 19 May 2021

References

- Duan, H. et al. Ultrathin rhodium nanosheets. *Nat. Commun.* **5**, 3093 (2014).
- Liu, D. et al. Three-dimensional controlled growth of monodisperse sub-50 nm heterogeneous nanocrystals. *Nat. Commun.* **8**, 10254 (2016).
- Wiley, B., Sun, Y. & Xia, Y. Synthesis of silver nanostructures with controlled shapes and properties. *Acc. Chem. Res.* **40**, 1067–1076 (2007).
- Peng, X. et al. Shape control of CdSe nanocrystals. *Nature* **404**, 59–61 (2000).
- Yin, Y. & Alivisatos, A. P. Colloidal nanocrystal synthesis and the organic–inorganic interface. *Nature* **437**, 664–670 (2005).
- Jonathan, O. et al. The coordination chemistry of nanocrystal surfaces. *Science* **347**, 615–616 (2015).
- Kim, Y. et al. Transmutable nanoparticles with reconfigurable surface ligands. *Science* **351**, 579–582 (2016).
- Xia, Y. et al. Self-assembly of self-limiting monodisperse superparticles from polydisperse nanoparticles. *Nat. Nanotechnol.* **6**, 580–587 (2011).
- Zhang, S. et al. An all-inorganic colloidal nanocrystal flexible polarizer. *Angew. Chem. Int. Ed.* **58**, 8730–8735 (2019).
- Lv, J. et al. Gold nanowire chiral ultrathin films with ultrastrong and broadband optical activity. *Angew. Chem. Int. Ed.* **129**, 5137–5142 (2017).
- Lv, J. et al. Biomimetic chiral photonic crystals. *Angew. Chem. Int. Ed.* **58**, 7783–7787 (2019).
- Bai, F. et al. A versatile bottom-up assembly approach to colloidal spheres from nanocrystals. *Angew. Chem. Int. Ed.* **119**, 6770–6773 (2007).
- Salaita, K., Wang, Y. & Mirkin, C. A. Applications of dip-pen nanolithography. *Nat. Nanotechnol.* **2**, 145–155 (2007).
- Ciszek, J. W. et al. Kinetically controlled, shape-directed assembly of nanorods. *Small* **4**, 206–210 (2008).
- Dong, A. et al. A generalized ligand-exchange strategy enabling sequential surface functionalization of colloidal nanocrystals. *J. Am. Chem. Soc.* **133**, 998–1006 (2011).
- Dubois, F. et al. A versatile strategy for quantum dot ligand exchange. *J. Am. Chem. Soc.* **129**, 482–483 (2007).
- Wang, X. et al. A general strategy for nanocrystal synthesis. *Nature* **437**, 121–124 (2005).
- Dai, X. et al. Quantum-dot light-emitting diodes for large-area displays: towards the dawn of commercialization. *Adv. Mater.* **29**, 1607022 (2017).
- Deng, R. et al. Intracellular glutathione detection using MnO_2 -nanosheet-modified upconversion nanoparticles. *J. Am. Chem. Soc.* **133**, 20168–20171 (2011).
- Qiao, R. et al. Ultrasensitive in vivo detection of primary gastric tumor and lymphatic metastasis using upconversion nanoparticles. *ACS Nano* **9**, 2120–2129 (2015).
- Carion, O. et al. Synthesis, encapsulation, purification and coupling of single quantum dots in phospholipid micelles for their use in cellular and in vivo imaging. *Nat. Protoc.* **2**, 2383–2390 (2007).

22. Melo-Diogo, D. D. et al. Strategies to improve cancer photothermal therapy mediated by nanomaterials. *Adv. Healthcare Mater.* **6**, 1700073 (2017).
23. Lin, Q. et al. Building superlattices from individual nanoparticles via template-confined DNA-mediated assembly. *Science* **359**, 669–672 (2018).
24. Ge, H. et al. Sequence-dependent DNA functionalization of upconversion nanoparticles and their programmable assemblies. *Angew. Chem. Int. Ed.* **59**, 8133–8137 (2020).
25. Kuzyk, A. et al. DNA-based self-assembly of chiral plasmonic nanostructures with tailored optical response. *Nature* **483**, 311–314 (2012).
26. Xue, J. et al. Surface ligand management for stable FAPbI₃ perovskite quantum dot solar cells. *Joule* **2**, 1866–1878 (2018).
27. Zhang, X. et al. Inorganic CsPbI₃ perovskite coating on PbS quantum dot for highly efficient and stable infrared light converting solar cells. *Adv. Energy Mater.* **8**, 1702049 (2018).
28. Liu, B. et al. Ligand-free noble metal nanocluster catalysts on carbon supports via “soft” nitriding. *J. Am. Chem. Soc.* **138**, 4718–4721 (2016).
29. Lu, H. & Jiang, Q. Size-dependent surface energies of nanocrystals. *J. Phys. Chem. B* **108**, 5617–5619 (2004).
30. Bogdan, N. et al. Synthesis of ligand-free colloidal stable water dispersible brightly luminescent lanthanide-doped upconverting nanoparticles. *Nano Lett.* **11**, 835–840 (2011).
31. Gai, S., Li, C., Yang, P. & Lin, J. Recent progress in rare earth micro/nanocrystals: soft chemical synthesis, luminescent properties, and biomedical applications. *Chem. Rev.* **114**, 2343–2389 (2014).
32. Pearson, G. R. et al. Hard and soft acids and bases. *J. Am. Chem. Soc.* **85**, 3533–3539 (1963).
33. Zhao, F. et al. Monodisperse lanthanide oxysulfide nanocrystals. *J. Am. Chem. Soc.* **128**, 11758–11759 (2006).
34. Yuan, Z. et al. Paving metal-organic frameworks with upconversion nanoparticles via self-assembly. *J. Am. Chem. Soc.* **140**, 15507–15515 (2018).
35. Lu, C. & Tang, Z. Advanced inorganic nanoarchitectures from oriented self-assembly. *Adv. Mater.* **28**, 1096–1108 (2016).
36. Tang, Z., Kotov, N. A. & Giersig, M. Spontaneous organization of single CdTe nanoparticles into luminescent nanowires. *Science* **297**, 237–240 (2002).
37. Tang, Z., Zhang, Z., Wang, Y., Glotzer, S. C. & Kotov, N. A. Self-assembly of CdTe nanocrystals into free-floating sheets. *Science* **314**, 274–278 (2006).
38. You, W. et al. Lanthanide-doped disordered crystals: site symmetry and optical properties. *J. Lumin.* **201**, 255–264 (2018).
39. Du, Y. et al. Highly luminescent self-organized sub-2-nm EuOF nanowires. *J. Am. Chem. Soc.* **131**, 16364–16365 (2009).
40. Tu, D. et al. Breakdown of crystallographic site symmetry in lanthanide-doped NaYF₄. *Angew. Chem. Int. Ed.* **52**, 1128–1133 (2013).
41. Liu, L. & Chen, X. Energy levels, fluorescence lifetime and Judd–Ofelt parameters of Eu³⁺ in Gd₂O₃ nanocrystals. *Nanotechnology* **18**, 255704 (2007).
42. Yang, Y. et al. Scalable assembly of crystalline binary nanocrystal superparticles and their enhanced magnetic and electrochemical properties. *J. Am. Chem. Soc.* **140**, 15038–15047 (2018).
43. Yeom, J. et al. Chiral templating of self-assembling nanostructures by circularly polarized light. *Nat. Mater.* **14**, 66–72 (2015).
44. Werts, M. H. V., Jukes, R. T. F. & Verhoeven, J. W. The emission spectrum and the radiative lifetime of Eu³⁺ in luminescent lanthanide complexes. *Phys. Chem. Chem. Phys.* **4**, 1542–1548 (2002).
45. Forster, T. Zwischenmolekulare energiewanderung und fluoreszenz. *Ann. Phys.* **437**, 55–75 (1948).
46. Rabouw, F. T., Den Hartog, S. A., Senden, T. & Meijerink, A. Photonic effects on the Forster resonance energy transfer efficiency. *Nat. Commun.* **5**, 3610 (2014).
47. Omagari, S. et al. Critical role of energy transfer between terbium ions for suppression of back energy transfer in nonanuclear terbium clusters. *Sci. Rep.* **6**, 37008 (2016).
48. Kasprzycka, E. Contribution of energy transfer from the singlet state to the sensitization of Eu³⁺ and Tb³⁺ luminescence by Sulfonylamidophosphates. *Chem.-Eur. J.* **23**, 1318–1330 (2017).
49. Wen, S. et al. Advances in highly doped upconversion nanoparticles. *Nat. Commun.* **9**, 2415 (2018).

Acknowledgements

This work was supported by the Major Research Program Cultivation Project of National Science Foundation of China (Grant No.: 91956107) and the National Science Foundation of China (Grant No.: 21371095).

Author contributions

L.H. initiated and led this research. J.Z. and Y.We. contributed equally to this work. The manuscript was written through the contributions of all authors. All authors gave approval to the final version of the manuscript. L.H., J.Z. and Y.We. designed the experimental approaches. J.Z., Y.We., Y.Wa. and F.Z. performed the experiments. L.H., J.Z., Y.We., Y.P., Z.Y., H.So., J.Y., H.Su. and X.X. analyzed the data. L.H., J.Z. and Y.We. wrote the manuscript.

Competing interests

The authors declare no competing interests.

Additional information

Supplementary information The online version contains supplementary material available at <https://doi.org/10.1038/s41467-021-23176-y>.

Correspondence and requests for materials should be addressed to X.X. or L.H.

Peer review information *Nature Communications* thanks the anonymous reviewer(s) for their contribution to the peer review of this work.

Reprints and permission information is available at <http://www.nature.com/reprints>

Publisher's note Springer Nature remains neutral with regard to jurisdictional claims in published maps and institutional affiliations.



Open Access This article is licensed under a Creative Commons Attribution 4.0 International License, which permits use, sharing, adaptation, distribution and reproduction in any medium or format, as long as you give appropriate credit to the original author(s) and the source, provide a link to the Creative Commons license, and indicate if changes were made. The images or other third party material in this article are included in the article's Creative Commons license, unless indicated otherwise in a credit line to the material. If material is not included in the article's Creative Commons license and your intended use is not permitted by statutory regulation or exceeds the permitted use, you will need to obtain permission directly from the copyright holder. To view a copy of this license, visit <http://creativecommons.org/licenses/by/4.0/>.

© The Author(s) 2021